ARTICLE IN PRESS

European Journal of Mechanics B/Fluids ▮ (▮▮▮▮) ▮▮▮–▮▮▮

Contents lists available at ScienceDirect

European Journal of Mechanics B/Fluids

journal homepage: www.elsevier.com/locate/ejmflu

Numerical and experimental study of pressure-wave formation around an underwater ventilated vehicle

Xiaoshi Zhang [a], Cong Wang [a,*], David Wafula Wekesa [a,b]

[a] School of Astronautics, Harbin Institute of Technology, Harbin 150001, China

[b] Department of Physics, Jomo Kenyatta University of Agriculture & Technology, Nairobi City, Kenya

ARTICLE INFO

Article history:
Received 6 January 2016
Received in revised form
23 June 2016
Accepted 23 January 2017
Available online xxxx

Keywords:
Cavitation
Turbulence
Ventilated cavitation flows
Re-entrant jet
Filter-based turbulence model

ABSTRACT

The objective of this study was to understand better the ventilated cavitation flow structure around an underwater ventilated vehicle. A high-speed camera system was used to observe the cavity evolution of unsteady cavitation flow, and a dynamic pressure measurement system was used to measure the instantaneous pressure during cavity growth. The numerical simulation is presented using the secondary development of computational fluid dynamics code CFX with a filter-based turbulence model. The results indicate that the ventilated flow rate of the gas influences the development of ventilated cavitation, and the pressure fluctuation is suppressed remarkably by the ventilated cavity evolution. The results also indicate that the proposed method can effectively capture the unsteady cavitation structure in accordance with the quantitative features observed in the experiment. It can therefore be concluded that the pressure fluctuations are induced by the vortex because of its periodic shedding toward downstream. The vortex shedding causes changes in the pressure distribution on the vehicle surface. Some secondary pressure oscillations can be observed that are attributable to the shedding of secondary vortex structures near the vehicle surface. These findings provide an important basis for facilitating the better understanding of the unsteady ventilated cavitation flows.

1. Introduction

Cavitation around the low-pressure region of an underwater vehicle is associated with the launching of a process of high-speed vehicle [1]. When a vehicle is exiting the water, the pressure fluctuations generated by the cavitation bubbles collapse, which has a great influence on the trajectory and vibration of the vehicle. The cavitation around an axisymmetric vehicle and hydrofoils was investigated in previous studies [2–4]. Scholars have discovered a complex phenomenon, that is shock waves and jets are produced when the cavitation bubble collapses. The collapses may damage the structures attributable to cavitation erosion. Most work has been done in recent years on this particular aspect. Rouse and McNown [5] conducted a series of experiments on the cavitation flows of an axisymmetric model. Vlasenko [6] investigated the hydrodynamics of axisymmetric bodies moving in water in supercavitation flow regime. The shedding evolution of ventilated unsteady partial cavitation was observed in a launching experiment [7]. De Lange [8] observed two-dimensional (2D) and three-dimensional (3D) cavities. The experimental results showed that the formation of a re-entrant flow is the main cause of unsteadiness. A mechanism of cavity unsteadiness was caused by a re-entrant flow at the end of the cavity [9–12]. Unsteady cavitation was investigated by different methods such as the light intensity comparison [13], double optical probe technique [14], the ultrasonic ultrasonography and laser Doppler velocimetry [15], and X-ray imaging [16,17]. Huang [18,19] and Hu [20–22] used high-speed video to observe the cavitation flows, and the velocity fields in a water tunnel were measured by particle image velocimetry for different cavitation conditions. A peak of pressure fluctuations was observed at the cavity closure. The peak magnitude increased with an increase in the cavity length. Although the cavitation process may not be avoided, it is not always an undesired phenomenon in fluid dynamics. During the past decade, the researchers tried their best to minimize the undesired effects of cavitation and maximize the advantage of cavitation. Ceccin [23] presented the recent advances of the use of partial and supercavities for drag reduction of underwater vehicles and surface ships moving in a liquid.

To help improve the understanding of the complex structures of cavitation flows, various numerical methods have been proposed.

* Corresponding author.
E-mail address: hitzxs@gmail.com (C. Wang).

http://dx.doi.org/10.1016/j.euromechflu.2017.01.011
0997-7546/

Please cite this article in press as: X. Zhang, et al., Numerical and experimental study of pressure-wave formation around an underwater ventilated vehicle, European Journal of Mechanics B/Fluids (2017), http://dx.doi.org/10.1016/j.euromechflu.2017.01.011

In the CFD framework for cavitation simulation, different kinds of two-phase flow approaches have been developed. A bubble two-phase flow model was developed by Kubota et al. [24] that can explain the interactions between cavitation and vortices. Singhal [25] provided a vapor mass fraction equation with pressure-dependent source terms to simulate cavitation flows in hydrofoils and orifices. Moreover, Sighal [26] employed a mathematical approach to derive a correlation for "full cavitation model" in which all the first-order effects were considered. Merkle [27] deployed a two-species adding compressibility effect equation to analyze the natural cavitation. Besides, Kunz [28] presented an implicit algorithm to compute the viscous two-phase flows and applied the algorithm to different models. Lindau et al. [29] and Kim et al. [30] adopted the Kunz model to study the unsteady 3D features of the cavitation flows over axisymmetric models with hemispheric and blunt noses. Senocak and Shyy [31] employed the pressure-based method for computing the turbulent sheet cavitation flows. A three-component model was proposed that considered the gas ventilation for simulating the natural and ventilated cavitation around an underwater vehicle [32,33]. In the numerical modeling of cavitation flows, the turbulence model determines the unsteady behavior of cavitation flows. The Reynolds-averaged Navier–Stokes (RANS) turbulence model is mostly used for single phase; however, some modifications [34] are required to make it suitable for compressible two-phase mixture flows. To better capture the unsteady features, sheet/cloud cavitation structures on the hydrofoils and ventilated cavitation are simulated by a large eddy simulation model [35–37]. The present work is a study of ventilation cavitation flow structure using the filter-based turbulence model (FBM). The FBM through unsteady simulations was assessed with the experimental data. The simulation results showed that the FBM could effectively capture the transient turbulence structures than that by the standard RANS models [38]. The ventilated cavitation flow on gas leakage behavior and re-entrant jet dynamics were investigated by combining numerical methods and experimental methods. A high-speed video camera was used to capture cavitation flows. The numerical simulation was performed by CFX with a free surface model and the FBM [39].

Most researchers focus on the cavity shedding mechanisms of unsteady cavitation flows over different models. However, few pay attention to the evolution of cavity and pressure after the beginning of ventilation over a vehicle. Therefore, in the present study, the unsteady ventilated cavitation flows over an underwater vehicle is investigated by an experimental method combined with a numerical method. Emphasis is placed on the real-time changes in cavity and pressure by experiment. The mechanism and flow structure in the unsteady ventilated cavitation are shown by numerical analysis to facilitate better understanding of the unsteady ventilated cavitation flows.

2. Description of numerical methods

2.1. Conservation of mass and momentum

In the mixture model of the multiphase flow, the governing continuity and momentum equations for a classical RANS and the homogeneous mixture multiphase flow equation shown are as follows:

$$\frac{\partial \rho_m}{\partial t} + \frac{\partial \left(\rho_m u_j\right)}{\partial x_j} = 0; \tag{1}$$

$$\frac{\partial(\rho_m u_i)}{\partial t} + \frac{\partial(\rho_m u_i u_j)}{\partial x_j} = \rho f_i - \frac{\partial p}{\partial x_i} + \frac{\partial}{\partial x_j} \times \left[(\mu_m + \mu_t)\left(\frac{\partial u_i}{\partial x_j} + \frac{\partial u_j}{\partial x_i} - \frac{2}{3}\frac{\partial u_i}{\partial x_j}\delta_{ij}\right)\right]. \tag{2}$$

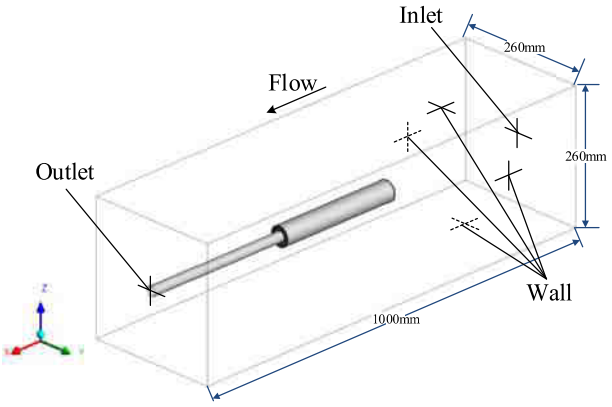

Fig. 1. Computation domain and boundaries.

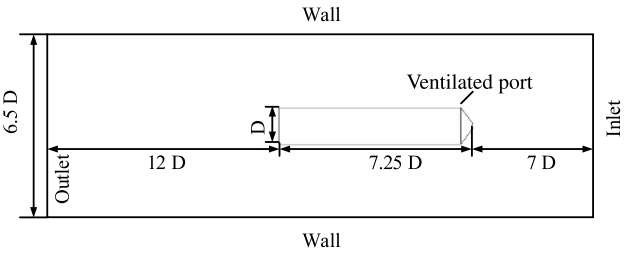

Fig. 2. Sketch of the test body's position in the test section.

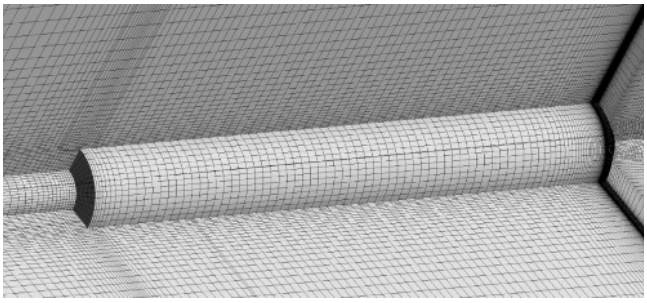

Fig. 3. Mesh generation around the vehicle surface.

The subscripts i, j, and k represent the axes directions of the axes, u is the velocity, p is the mixture pressure, and μ_t is the turbulent viscosity [40]; the mixture density ρ_m and the mixture laminar viscosity μ_m are defined as

$$\rho_m = \sum_{k=1}^{n} \alpha_k \rho_k; \qquad \mu_m = \sum_{k=1}^{n} \alpha_k \mu_k \tag{3}$$

where α_k is the volume fraction of phase k, n is the number of phases.

2.2. Filter-based turbulence model

The numerical simulation is presented by the secondary development of computational fluid dynamics code CFX by using an FBM. The filter turbulence fields use a modified form of the standard $k-\varepsilon$ [41] turbulence model shown as follows:

$$\frac{\partial(\rho k)}{\partial t} + \frac{\partial(\rho u_i k)}{\partial x_j} = P_k - \rho\varepsilon + \frac{\partial}{\partial x_j}\left[\left(\mu + \frac{\mu_t}{\sigma_k}\right)\frac{\partial k}{\partial x_j}\right]; \tag{4}$$

Please cite this article in press as: X. Zhang, et al., Numerical and experimental study of pressure-wave formation around an underwater ventilated vehicle, European Journal of Mechanics B/Fluids (2017), http://dx.doi.org/10.1016/j.euromechflu.2017.01.011

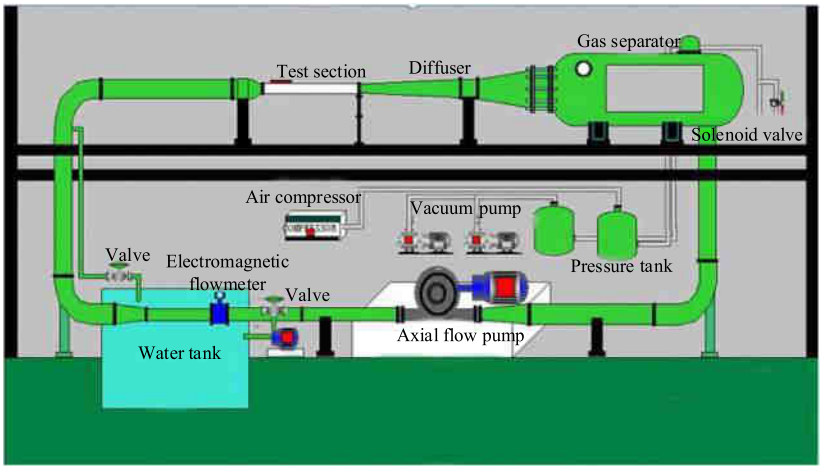

Fig. 4. Schematic of the water tunnel.

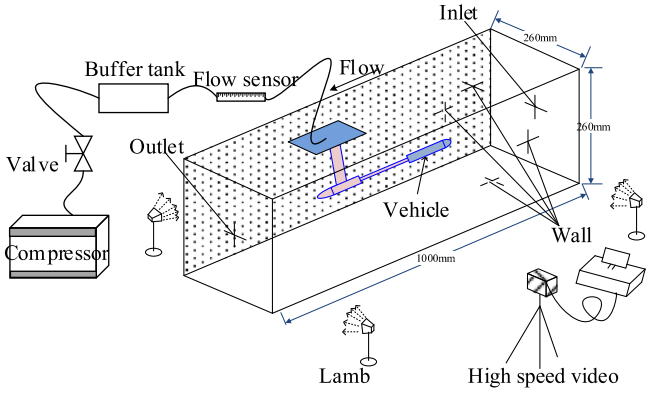

Fig. 5. Schematic of the test section.

$$\frac{\partial(\rho\varepsilon)}{\partial t}+\frac{\partial(\rho u_j\varepsilon)}{\partial x_j} = C_{\varepsilon 1}\frac{\varepsilon}{k}P_k - C_{\varepsilon 2}\rho\frac{\varepsilon^2}{k}+\frac{\partial}{\partial x_j} \times\left[\left(\mu+\frac{\mu_t}{\sigma_\varepsilon}\right)\frac{\partial\varepsilon}{\partial x_j}\right]. \tag{5}$$

In our model, however, the two turbulence fields represent conditionally ensemble averaged and filtered values, facilitated by the definition of the eddy viscosity, and in the limit of coarse filters and slow transient flows, the standard $k-\varepsilon$ turbulence model is recovered. The turbulent energy production (P_t) and the Reynolds stress tensor terms (τ_{ij}) are defined as

$$P_t=\tau_{ij}\frac{\partial u_i}{\partial x_j};\quad \tau_{ij}=\frac{2}{3}\rho_m k\delta_{ij}-\mu_T\left(\frac{\partial u_i}{\partial x_j}+\frac{\partial u_j}{\partial x_i}\right) \tag{6}$$

where $C_{\varepsilon 1}=1.44$, $C_{\varepsilon 2}=1.92$, $\sigma_\varepsilon=1.3$, and $\sigma_k=1.0$. The turbulent eddy viscosity is defined as

$$\mu_t=\frac{C_\mu\rho k^2}{\varepsilon},\quad C_\mu=0.09. \tag{7}$$

Johansen [42] proposed a special filter to help reduce μ_t; if the turbulent scales are smaller than the set filter size, they will not be resolved. Specifically, the level of the turbulent viscosity is corrected by comparing the turbulence length scale and the filter size Δ, which is selected depending on the local meshing spacing

$$\mu_t=\frac{C_\mu\rho k^2}{\varepsilon}F,\quad C_\mu=0.09$$
$$F=\mathrm{Min}\left[1, C_3\frac{\Delta\cdot\varepsilon}{k^{3/2}}\right],\quad C_3=1.0 \tag{8}$$

when $\Delta\gg k^{3/2}/\varepsilon$, Eq. (8) yields $\mu_t=C_\mu\rho k^2/\varepsilon$, and we recover the standard $k-\varepsilon$ model when $\Delta\ll k^{3/2}\varepsilon$ and $\mu_t=C_\mu\rho\cdot\Delta\cdot k^{1/2}$.

2.3. Numerical set-up and description

Fig. 1 shows the shape of the vehicle and the computational domain. The rectangular cross-section has a height of 260 mm and a width of 260 mm. The diameter of the cylindrical part of the vehicles is $D=40$ mm and the length of the vehicle

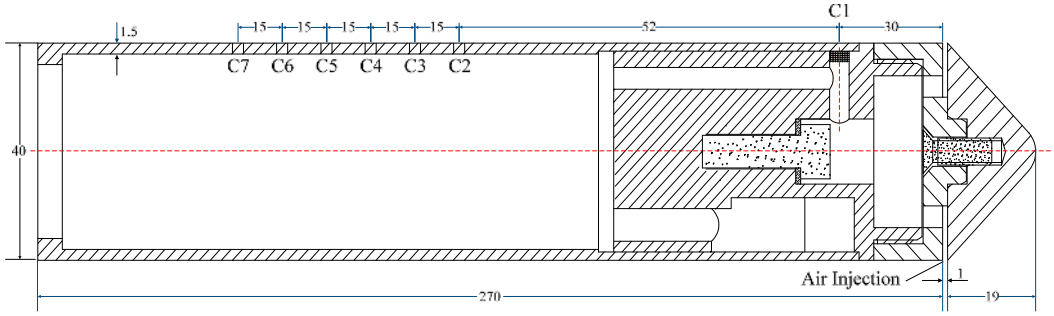

Fig. 6. Cross-section of the test body.

Please cite this article in press as: X. Zhang, et al., Numerical and experimental study of pressure-wave formation around an underwater ventilated vehicle, European Journal of Mechanics B/Fluids (2017), http://dx.doi.org/10.1016/j.euromechflu.2017.01.011

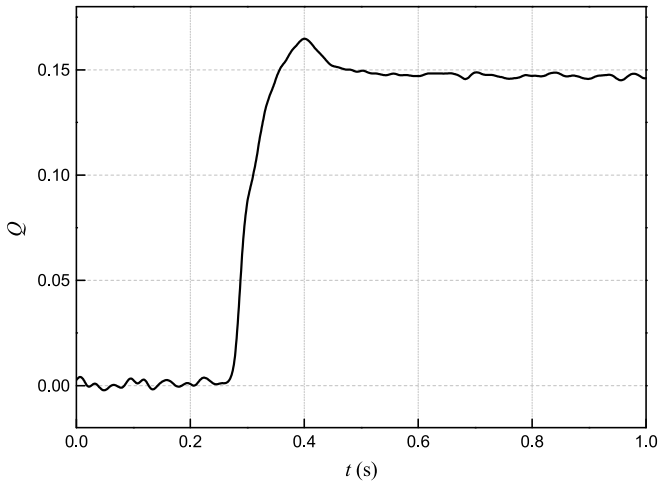

Fig. 7. Gas entrainment coefficient with respect to time.

is $L = 7.25D$. The upper and lower boundaries are located at $3.25D$ from the center of the vehicle nose. The boundaries of the upstream and the downstream are located at $12D$ and $7D$ as shown in Fig. 2. The boundary conditions are as follows: uniform velocity at the domain inlet and static pressure at the outlet, and wall conditions at other domain sides. The vehicles body and the lateral boundaries assume the no-slip wall conditions. The structured meshes were adopted in the calculation. The computation grid is more concentrated near the vehicle surface and air injection ports. After a grid independency solution study, a 530,000 mesh is used for all computations around the vehicle. The fine 3D fluid mesh is shown in Fig. 3.

3. Experimental set-up

The experiments were conducted in the high-speed water tunnel of the Harbin Institute of Technology. The schematic of the water tunnel is shown in Fig. 4. The water tunnel is a closed jet with recirculating facility, and the velocities can be higher than 18 m/s. The tunnel allows for removing a great quantity of air during ventilation experiments by a special design. The test section

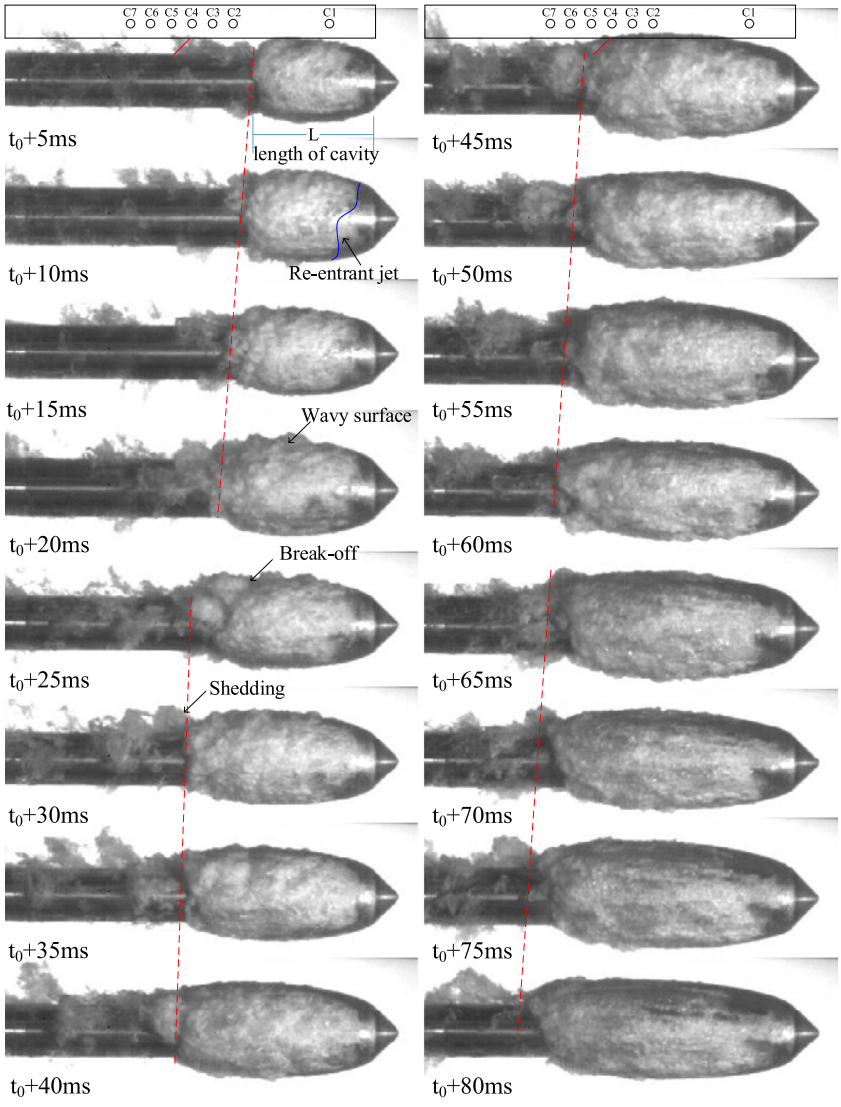

Fig. 8. Evolution of the cavity shape.

Please cite this article in press as: X. Zhang, et al., Numerical and experimental study of pressure-wave formation around an underwater ventilated vehicle, European Journal of Mechanics B/Fluids (2017), http://dx.doi.org/10.1016/j.euromechflu.2017.01.011

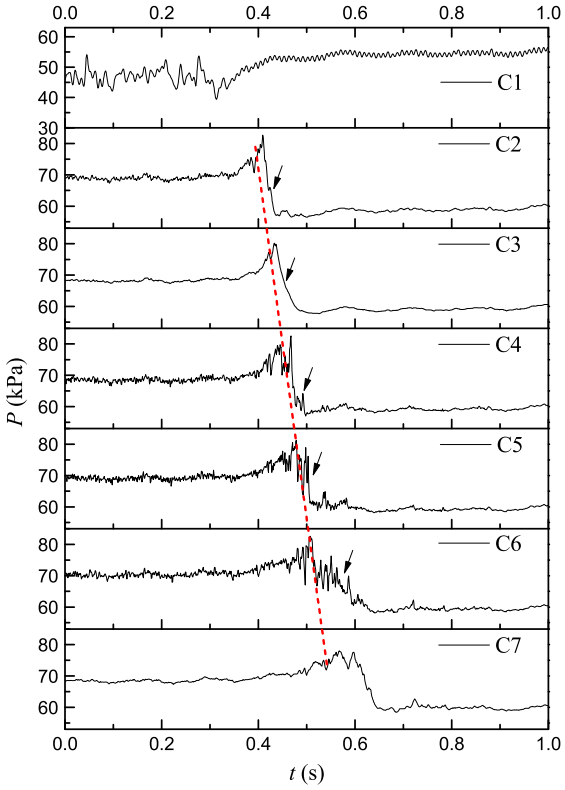

Fig. 9. Instantaneous pressure signals during cavity growth.

is a channel of 260 × 260-mm rectangular cross-section and 1000-mm length with flat parallel sidewalls. The sidewalls of the test section are equipped with transparent windows to perform visual observations, and the air injection system is used as shown in Fig. 5. The main components of the test section are compressor, pressure regulating valve, and flow sensor. In this system, the ventilation pressure and the gas entrainment coefficient can be measured by the flow sensors.

The test vehicle is mounted in the tunnel. The length of the test body is $L = 335$ mm, and the diameter is $D = 40$ mm. A schematic of the test body is shown in Fig. 6. The surface pressure at different locations on the model is also measured to aid the understanding of the observed flow physics. Seven CYG505 transducer conditioners were embedded in the model to facilitate the unsteady pressure measurements. The pressure transducers' locations are shown in Fig. 6. The cavitation flow around the model was imaged with a Photron FASTCAM SA-X high-speed video camera. The velocity at the inlet of the test section was fixed at $U_0 = 8$ m/s, and the pressure upstream of the vehicle at the inlet was 68.4 kPa. The camera and the data acquisition system are triggered simultaneously.

4. Results and discussion

The unsteady cavitaton flows around the vehicle are investigated by both experimental and numerical methods. The gas entrainment coefficient quantifies the gas required in the nondimensional form, which is given introduced by [43,44]

$$Q = \frac{\dot{Q}}{V_\infty D_n^2}$$

where $\dot{Q}$ is the volume flow rate of the injected gas. The values of the gas entrainment coefficient Q with respect to time are shown in Fig. 7. Thus, in the numerical simulation process, the air injection is adjusted according to the dimensionless coefficient of the rate.

4.1. Evolution of cavitation pattern

To study the evolution of cavity and pressure after the beginning of ventilation over a vehicle, the unsteady ventilated cavitation flows over an underwater vehicle are investigated by an experimental method.

The experimental evolution of the ventilated cavitation from the start of the ventilation until the ventilated cavity length stops growing is shown in Fig. 8. The evolution of the cavity shape can be described as follows. At the beginning of the cycle, the cavity forms and grows gradually after the vehicle is ventilated at $t_0 + 5$ ms. The cavity and re-entry jet influence each other. The adverse pressure gradient becomes strong and overcomes the momentum of the flow confined in the near-wall region, and the re-entrant flow then forms at $t_0 + 10$ ms. The re-entrant jet moves into the cavity after its generation, and a partial re-entrant jet motion is observed. The unsteady re-entrant jet impinges on the cavity boundaries, and the cavity boundaries become wavy as shown in Fig. 8 ($t_0 + 20$ ms). A closer examination of the opaque regions reveals that the cavity surface is not smooth in these areas. From $t_0 + 20$ to $t_0 + 25$ ms, the cavity is cut by this reverse flow and forms sheet cavity, which is lifted away from the vehicle surface leading to cavity break-off. The break-off behavior becomes violent to cause the shedding cavity to roll up, and large cavity vortexes shed toward downstream. From $t_0 + 45$ to $t_0 + 80$ ms, the forefront of the transparent cavity forms a smooth interface. At this time, when the cavity length is half the vehicle, the increase in cavity length is more gradual and more fluctuating.

4.2. Wall-pressure fluctuations

Fig. 9 presents the instantaneous pressure signals during the cavity growth on the vehicle surface. The transducers on the surface pass alternately from the noncavitating pressure to the ventilated pressure, as shown in Fig. 8.

As the cavity grows, an increase in pressure fluctuations before falling to the ventilated pressure is revealed (see dashed lines in Fig. 9 for C2–C5) when the cavity closure passes over the pressure

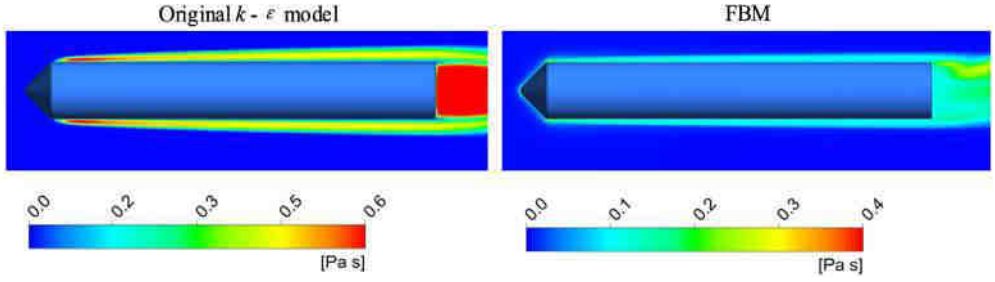

Fig. 10. Turbulence viscosity for different turbulence models.

Please cite this article in press as: X. Zhang, et al., Numerical and experimental study of pressure-wave formation around an underwater ventilated vehicle, European Journal of Mechanics B/Fluids (2017), http://dx.doi.org/10.1016/j.euromechflu.2017.01.011

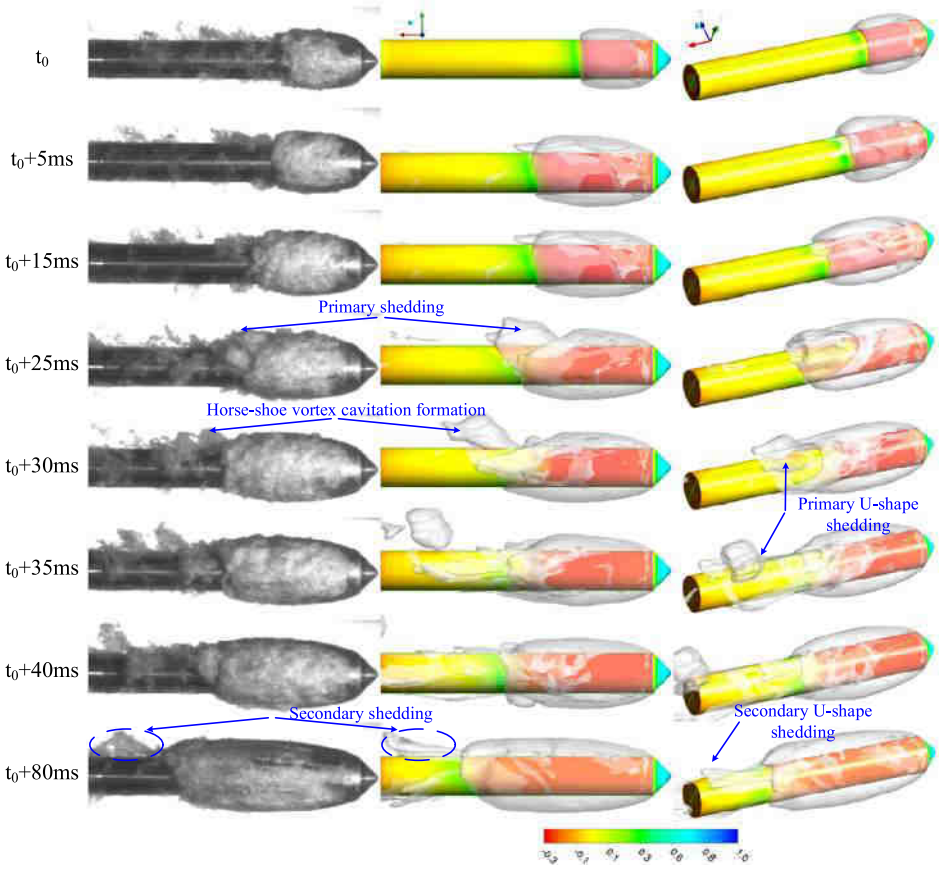

Fig. 11. Development of cavitation.

transducers one after another. It is observed that the pressure fluctuations are convected to the cavity wake. Then, a decrease in the pressure fluctuations is observed before the pressure falls to the ventilated pressure. The pressure decreases more gradually with more fluctuation (see arrows in Fig. 9 for C4 and C5) when the cavity length is half the vehicle. This corresponds to the re-entrant jet movement into the cavity. The pressure fluctuations are detected by the pressure transducer on the vehicle surface.

4.3. Flow structure in the rear part of the cavity

The modeling of turbulence plays an important role in the dynamics of the flow. An FBM originated from the $k-\varepsilon$ turbulence model [42] is first compared with the original $k-\varepsilon$ turbulence model [41] and assessed by the experimental data before being it is used.

To study the differences of the turbulence between the original $k-\varepsilon$ model and the FBM of a single-phase flow, their turbulence viscosities are compared. The turbulence viscosity around the ventilated vehicle is shown in Fig. 10. For the original $k-\varepsilon$ model, a higher eddy viscosity is predicted than that for the FBM.

Fig. 11 shows the numerical and experimental unsteady cavity evolution morphology around the vehicle at each stage. From the numerical results of the 3D view, the cavity shapes are extremely dissymmetrical along the vehicle. It indeed presents the 3D characteristics of the cavitation flows. The numerical results are shown in both the 2D and 3D views. The results show that the numerical predictions could capture the attached cavity with the growing cavity. The cavity break-off, the horse-shoe vortex structure with U-type shedding, and the secondary shedding are

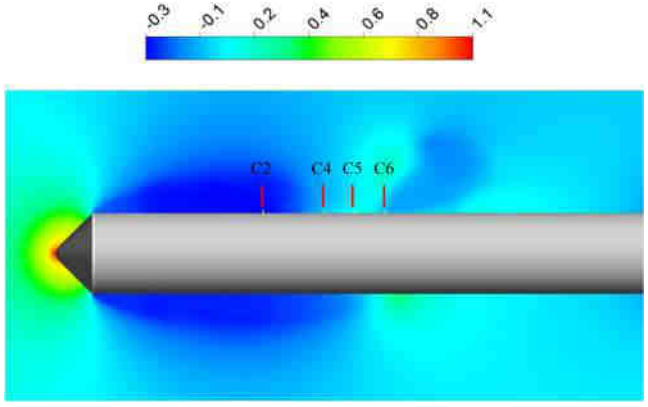

Fig. 12. Pressure coefficient contours, C2–C6 for comparison with experimental values.

in accordance with those observed in the experiment. Therefore, it is clear that the FBM can effectively capture the unsteady features.

To verify the computational results, the pressure fluctuations along the axisymmetric vehicle were compared with the experimental results as shown in Fig. 13. The monitor points indicate the location of transducers as shown in Fig. 12. It was found that the computed pressure fluctuations qualitatively follow the experimentally observed trend, and a good quantitative agreement in the cavitation number was observed. Although the differences between the simulated and the experimental data are more substantial with decrease in pressure, the agreement is reasonable considering the difficulties in experimental measurements and the compressibility effects of the numerical method.

Please cite this article in press as: X. Zhang, et al., Numerical and experimental study of pressure-wave formation around an underwater ventilated vehicle, European Journal of Mechanics B/Fluids (2017), http://dx.doi.org/10.1016/j.euromechflu.2017.01.011

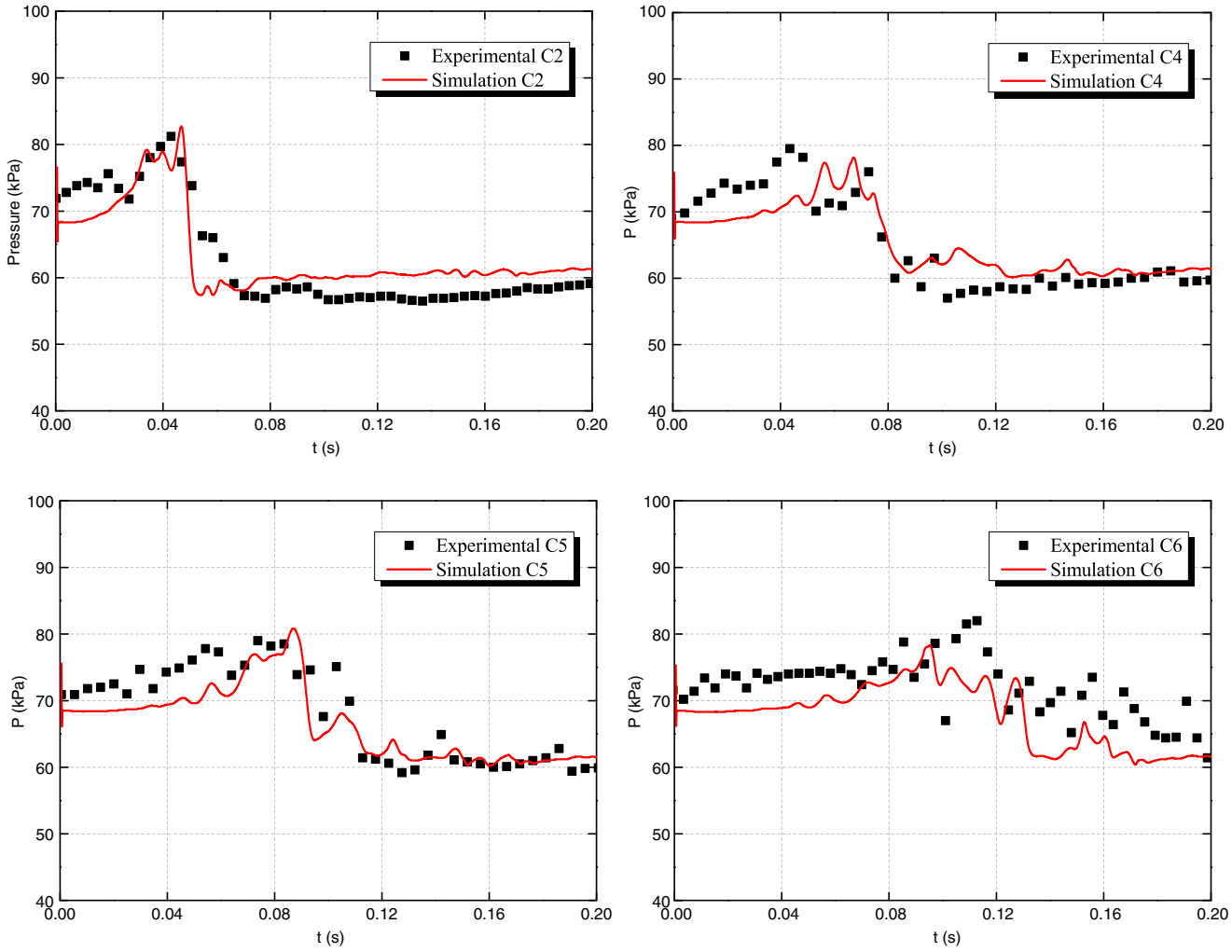

Fig. 13. Pressure fluctuations on the vehicle surface at C2, C4, C5, and C6.

4.4. Unsteady cloud cavitating vortex and the induced pressure

In ventilated cavitation flows, we can find that the pressure wave of the vehicle is highly correlated with the evolution of the vortex structures. Fig. 15 shows the time evolutions of the pressure coefficient on the vehicle surface with growing cavity. The instantaneous vortex and the pressure coefficient distributions are adopted to describe the flow field. It is obvious that the unsteady evolutions produced by the vortex shedding is the major reason for inducing the pressure wave. The flow structures at representative time instances ($T1 = t_0 + 15$ ms, $T2 = t_0 + 25$ ms, $T3 = t_0 + 30$ ms, and $T4 = t_0 + 35$ ms) are shown in Fig. 14. The instantaneous velocity vectors and the air volume fraction contours are used to investigate the unsteady vortex structures. To analyze the unsteady vortex better, pressure coefficient along the vehicle and vorticity are compared to show the hydrodynamic fluctuations. The relationship between the vortex structures and the pressure is given in the following paragraph.

The cavity grows until the re-entry flow appears. When the re-entry flow moves back to the front of the vehicle, the cavity separates from the vehicle. Fig. 14 shows the flow structures near the vehicle surface at representative time instances. At $T1 = t_0 +$ 15 ms, a vortex on the surface rotating clockwise is defined as V1. Low pressure is distributed at the core of vortex V1 and a high pressure on the vehicle surface because of the adverse pressure gradient as shown in Fig. 15(a). At $T2 = t_0 + 25$ ms, V1 leaves the vehicle surface, and the shedding vortex induces a local high pressure at the vehicle surface. The high pressure (D) at the vehicle surface and the low pressure (E) distributions at the core of vortex V1 sustain the adverse pressure gradient. It is necessary to form the second vortex structure rotating clockwise on the upper surface. The secondary vortex is defined as V2, which grows up because of the adverse pressure gradient. Then, vortex V1 moves downstream. It can also be found that the low-pressure area at the core of vortex V1 grows up. At $T3 = t_0 + 30$ ms cycle, vortex V2 leaves the cavity and vortex V3 grows up, which results in low-pressure distributions on the vehicle surface. In addition, vortex V2 becomes weak. A high pressure can be observed at the core of vortex V2. When the re-entry flow moves back to the front of the vehicle, the cavity breaks. At $T3 = t_0 + 30$ ms, the detached complex vortex structure can be observed near the rear part of the vehicle in Fig. 14(c). It is consistent with the detached cloud cavity. Break-up of the vortex structure induces local high pressure. Then, the high-pressure region extends rapidly. At $T4 = t_0 + 35$ ms, vortex V3 begins to move downstream because of the high-speed main flow out of the boundary layer. Then, the pressure at the core of vortex V3 decreases.

5. Conclusions

In the present study, the evolution of cavity and pressure-wave formation of the ventilated vehicle was experimentally and

Please cite this article in press as: X. Zhang, et al., Numerical and experimental study of pressure-wave formation around an underwater ventilated vehicle, European Journal of Mechanics B/Fluids (2017), http://dx.doi.org/10.1016/j.euromechflu.2017.01.011

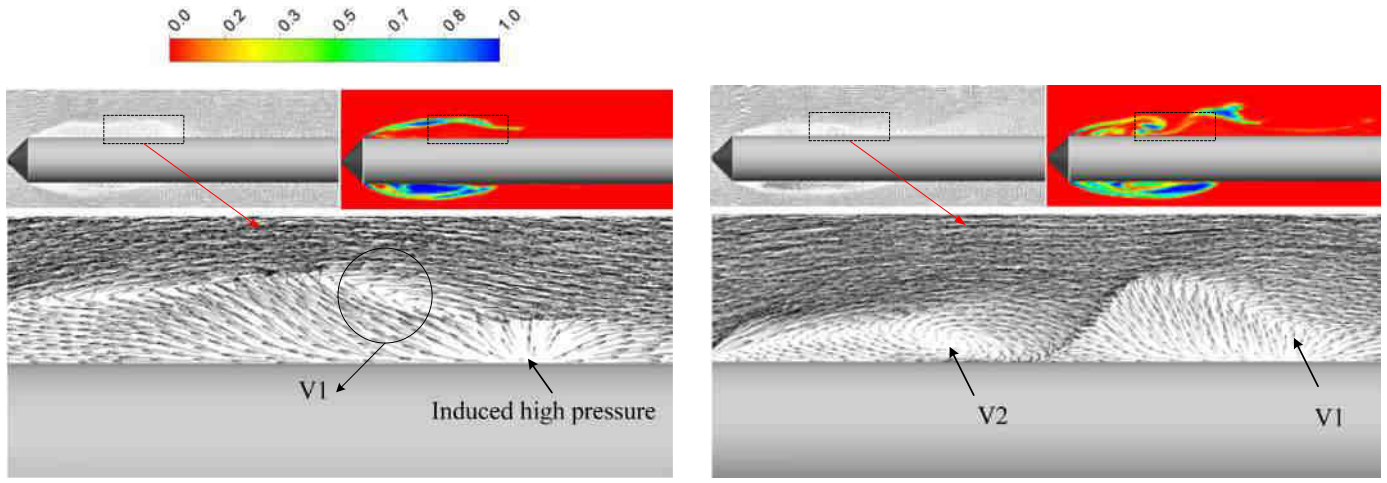

(a) $T1 = t_0 + 15$ ms.

(b) $T2 = t_0 + 25$ ms.

(c) $T3 = t_0 + 30$ ms.

(d) $T4 = t_0 + 35$ ms.

Fig. 14. Instantaneous velocity vectors and air volume fraction contours.

numerically investigated. The mechanism of ventilated partial cavitation was made clear through the photo analysis based on the high-speed video observation and the frame difference method. An FBM model from the standard $k - \varepsilon$ turbulence model was proposed to analyze the details of unsteady ventilated cavitation. The following conclusions can be drawn.

(1) The experimental results show that the evolutions of ventilated cavitation and the instantaneous pressure signals are observed during the cavity growth on the vehicle surface. It is observed that the pressure fluctuations are induced by the evolution of cavity, shedding, and collapse of the cavitation. The fluctuation pressure is located at the cavity closure depending on the cavitation number.

(2) The FBM model is used to reduce the eddy viscosity due to the lower filter function near the vehicle surface, which will lead to very different cavity dynamic processes, as compared to the experimental visualization results. In general, the predicted cavity dynamic results obtained using the FBM model with appropriate parameters are in good agreement with those from the experimental measurements and observations.

Please cite this article in press as: X. Zhang, et al., Numerical and experimental study of pressure-wave formation around an underwater ventilated vehicle, European Journal of Mechanics B/Fluids (2017), http://dx.doi.org/10.1016/j.euromechflu.2017.01.011

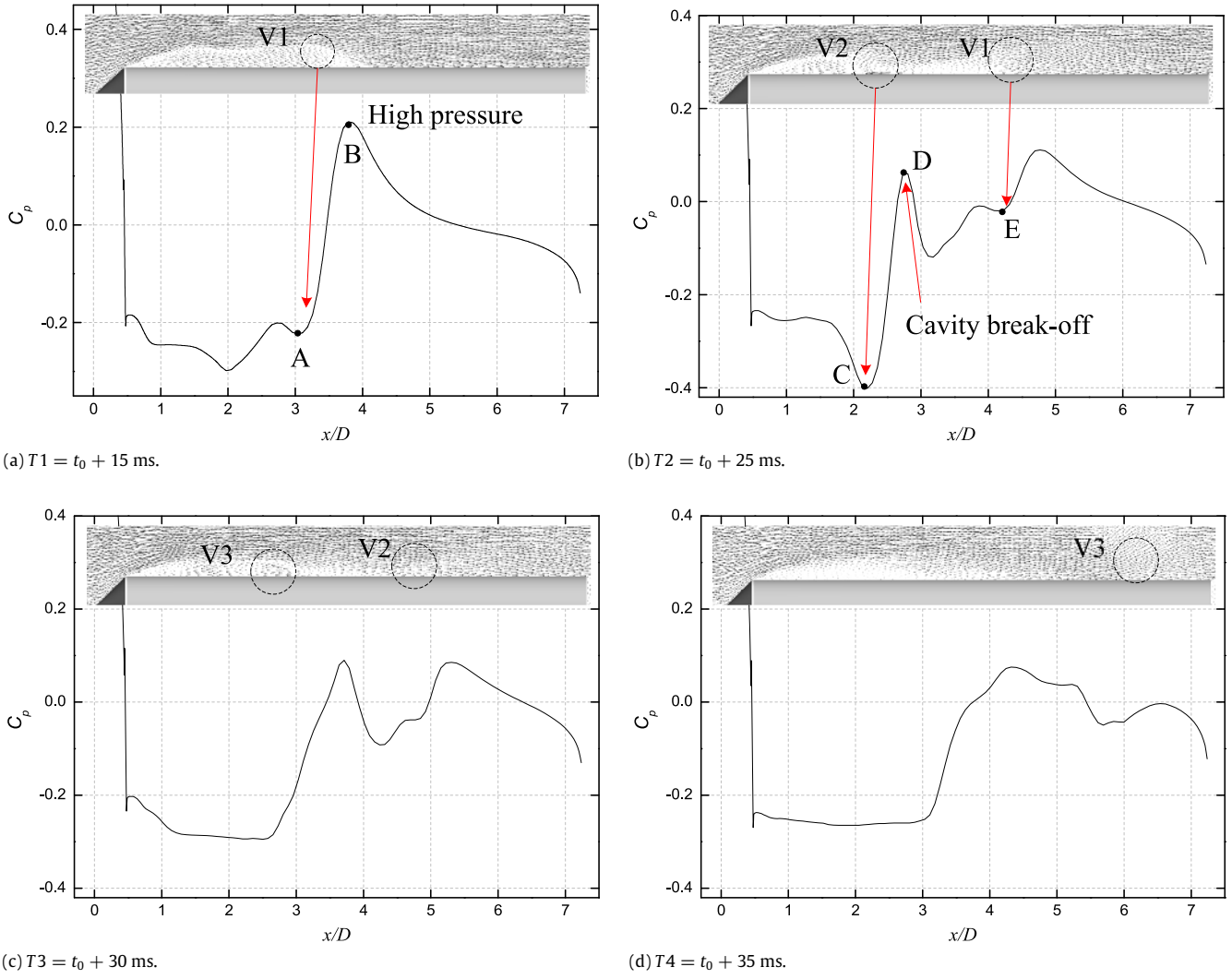

(a) $T1 = t_0 + 15$ ms. (b) $T2 = t_0 + 25$ ms.

(c) $T3 = t_0 + 30$ ms. (d) $T4 = t_0 + 35$ ms.

Fig. 15. Comparison between vorticity and distributions of the pressure coefficients along the vehicle surface.

(3) Vortex structure rotating clockwise sheds periodically into the wake region, which leads to changes in the pressure distribution on the vehicle surface. In addition, some secondary pressure oscillations can be observed, which are induced by the shedding of various vortex structures near the vehicle surface.

References

[1] J.R. Blake, D.C. Gibson, Cavitation bubbles near boundaries, Annu. Rev. Fluid Mech. 19 (1987) 99–123.
[2] R.E. Bensow, G. Bark, Implicit LES predictions of the cavitating flow on a propeller, ASME J. Fluids Eng. 132 (2010) 041302.
[3] O. Coutier Delgosha, F. Deniset, J.A. Astolfi, J.-B. Leroux, Numerical prediction of cavitating flow on a two-dimensional symmetrical hydrofoil and comparison to experiments, ASME J. Fluids Eng. 129 (2007) 279–292.
[4] F.M. Owis, A.H. Nayfeh, Numerical simulation of 3-D incompressible, multi-phase flows over cavitating projectiles, Eur. J. Mech. B Fluids 23 (2004) 339–351.
[5] H. Rouse, J.S. McNown, Cavitation and pressure distribution: head forms at zero angle of yaw, 1948.
[6] Y.D. Vlasenko, Experimental investigation of supercavitation flow regimes at subsonic and transonic speeds, in: Fifth International Symposium on Cavitation, Osaka, Japan, 2003.
[7] Y. Wang, C. Huang, T. Du, X. Wu, X. Fang, N. Liang, Y. Wei, Shedding phenomenon of ventilated partial cavitation around an underwater projectile, Chin. Phys. Lett. 29 (2012) 014601.
[8] D. De Lange, G. De Bruin, Sheet cavitation and cloud cavitation, re-entrant jet and three-dimensionality, in: Fascination of Fluid Dynamics, Springer, 1998, pp. 91–114.
[9] Y. Kawanami, H. Kato, H. Yamaguchi, M. Tanimura, Y. Tagaya, Mechanism and control of cloud cavitation, ASME J. Fluids Eng. 119 (1997) 788–794.
[10] J. Dang, G. Kuiper, Re-entrant jet modeling of partial cavity flow on two-dimensional hydrofoils, ASME J. Fluids Eng. 121 (1999) 773–780.
[11] R. Furness, S. Hutton, Experimental and theoretical studies of two-dimensional fixed-type cavities, ASME J. Fluids Eng. 97 (1975) 515–521.
[12] T. Pham, F. Larrarte, D. Fruman, Investigation of unsteady sheet cavitation and cloud cavitation mechanisms, ASME J. Fluids Eng. 121 (1999) 289–296.
[13] H. Sayyaadi, Instability of the cavitating flow in a venturi reactor, Fluid Dyn. Res. 42 (2010) 055503.
[14] B. Stutz, J. Reboud, Experiments on unsteady cavitation, Exp. Fluids 22 (1997) 191–198.
[15] M. Callenaere, J. Franc, J. Michel, M. Riondet, The cavitation instability induced by the development of a re-entrant jet, J. Fluid Mech. 444 (2001) 223–256.
[16] M. Dular, I. Khlifa, S. Fuzier, M.A. Maiga, O. Coutier-Delgosha, Scale effect on unsteady cloud cavitation, Exp. Fluids 53 (2012) 1233–1250.
[17] B. Stutz, S. Legoupil, X-ray measurements within unsteady cavitation, Exp. Fluids 35 (2003) 130–138.
[18] B. Huang, Y.L. Young, G. Wang, W. Shyy, Combined experimental and computational investigation of unsteady structure of sheet/cloud cavitation, ASME J. Fluids Eng. 135 (2013) 071301.
[19] B. Huang, G. Wang, Experimental and numerical investigation of unsteady cavitating flows through a 2D hydrofoil, Sci. China Technol. Sci. 54 (2011) 1801–1812.
[20] C. Hu, G. Wang, G. Chen, B. Huang, Three-dimensional unsteady cavitating flows around an axisymmetric body with a blunt headform, J. Mech. Sci. Technol. 29 (2015) 1093–1101.
[21] C. Hu, G. Wang, B. Huang, Experimental investigation on cavitating flow shedding over an axisymmetric blunt body, Chin. J. Mech. Eng. 28 (2015) 387–393.
[22] C. Hu, G. Wang, B. Huang, Y. Zhao, The inception cavitating flows over an axisymmetric body with a blunt head-form, J. Hydrodyn. Ser. B 27 (2015) 359–366.

Please cite this article in press as: X. Zhang, et al., Numerical and experimental study of pressure-wave formation around an underwater ventilated vehicle, European Journal of Mechanics B/Fluids (2017), http://dx.doi.org/10.1016/j.euromechflu.2017.01.011

[23] S.L. Ceccio, Friction drag reduction of external flows with bubble and gas injection, Annu. Rev. Fluid Mech. 42 (2010) 183–203.
[24] A. Kubota, H. Kato, H. Yamaguchi, A new modelling of cavitating flows: A numerical study of unsteady cavitation on a hydrofoil section, J. Fluid Mech. 240 (1992) 59–96.
[25] A. Singhal, N. Vaidya, A. Leonard, Multi-dimensional simulation of cavitating flows using a PDF model for phase change, ASME Paper FEDSM97-3272, 1997.
[26] A.K. Singhal, M.M. Athavale, H. Li, Y. Jiang, Mathematical basis and validation of the full cavitation model, J. Fluids Eng. 124 (2002) 617–624.
[27] C.L. Merkle, J. Feng, P.E. Buelow, Computational modeling of the dynamics of sheet cavitation, in: 3rd International Symposium on Cavitation, Grenoble, France, 1998, pp. 47–54.
[28] R.F. Kunz, D.A. Boger, D.R. Stinebring, T.S. Chyczewski, J.W. Lindau, H.J. Gibeling, S. Venkateswaran, T. Govindan, A preconditioned Navier–Stokes method for two-phase flows with application to cavitation prediction, Comput. & Fluids 29 (2000) 849–875.
[29] J.W. Lindau, R.F. Kunz, D.A. Boger, D.R. Stinebring, H.J. Gibeling, High Reynolds number, unsteady, multiphase CFD modeling of cavitating flows, J. Fluids Eng. 124 (2002) 607–616.
[30] D.-H. Kim, W.-G. Park, C.-M. Jung, Numerical simulation of cavitating flow past axisymmetric body, Int. J. Naval Archit. Ocean Eng. 4 (2012) 256–266.
[31] I. Senocak, W. Shyy, Numerical simulation of turbulent flows with sheet cavitation, 2001. http://resolver.caltech.edu/cav2001:sessionA7.002.
[32] B. Ji, X.-W. Luo, Y. Zhang, H.-J. Ran, H.-Y. Xu, Y.-L. Wu, A three-component model suitable for natural and ventilated cavitation, Chin. Phys. Lett. 27 (2010) 096401.
[33] B. Ji, X.-W. Luo, X.-X. Peng, Y. Zhang, Y.-L. Wu, H.-Y. Xu, Numerical investigation of the ventilated cavitating flow around an under-water vehicle based on a three-component cavitation model, J. Hydrodyn. Ser. B 22 (2010) 753–759.
[34] E. Goncalvès, Numerical study of unsteady turbulent cavitating flows, Eur. J. Mech. B Fluids 30 (2011) 26–40.
[35] G. Wang, M. Ostoja-Starzewski, Large Eddy simulation of a sheet/cloud cavitation on a NACA0015 hydrofoil, Appl. Math. Model. 31 (2007) 417–447.
[36] B. Ji, X. Luo, R.E. Arndt, X. Peng, Y. Wu, Large Eddy simulation and theoretical investigations of the transient cavitating vortical flow structure around a NACA66 hydrofoil, Int. J. Multiph. Flow 68 (2015) 121–134.
[37] Y. Wang, C. Huang, X. Fang, X. Yu, X. Wu, T. Du, On the cloud cavitating flow over a submerged axisymmetric projectile and comparison between 2D RANS and 3D LES methods, J. Fluids Eng. (2015).
[38] J. Wu, G. Wang, W. Shyy, Time-dependent turbulent cavitating flow computations with interfacial transport and filter-based models, Internat. J. Numer. Methods Fluids 49 (2005) 739–761.
[39] Z. Wang, B. Huang, G. Wang, M. Zhang, F. Wang, Experimental and numerical investigation of ventilated cavitating flow with special emphasis on gas leakage behavior and re-entrant jet dynamics, Ocean Eng. 108 (2015) 191–201.
[40] R.S. Rogallo, P. Moin, Numerical simulation of turbulent flows, Annu. Rev. Fluid Mech. 16 (1984) 99–137.
[41] B.E. Launder, D. Spalding, The numerical computation of turbulent flows, Comput. Methods Appl. Math. 3 (1974) 269–289.
[42] S.T. Johansen, J. Wu, W. Shyy, Filter-based unsteady RANS computations, Int. J. Heat Fluid Flow 25 (2004) 10–21.
[43] G. Logvinovich, Hydrodynamics of Flows with Free Boundaries, Naukova Dumka, Kiev, 1969, p. 128.
[44] L. Epshtein, Methods of Theory of Dimensionality and Similarity in Problems of Ship Hydromechanics, Sudostroenie Publishing House, Leningrad, 1970.

Please cite this article in press as: X. Zhang, et al., Numerical and experimental study of pressure-wave formation around an underwater ventilated vehicle, European Journal of Mechanics B/Fluids (2017), http://dx.doi.org/10.1016/j.euromechflu.2017.01.011